ACS OMEGA

Open Access

http://pubs.acs.org/journal/acsodf

Article

Impact of Crystallite Size and Phase Boundaries on Magnetic and Thermoelectric Properties of Cu-Added $BiFeO_3$

Krishnamoorthy Aishwarya, Selvam Maruthasalamoorthy, Ramalingam Thenmozhi, Jayaraman Mani, Gopalakrishnan Anbalagan, Rajkumar Nirmala, Mani Navaneethan, and Navamathavan Rangaswamy*

Cite This: *ACS Omega* 2024, 9, 35088−35099

Read Online

ACCESS | Metrics & More | Article Recommendations | Supporting Information

ABSTRACT: In this study, bismuth ferrite (BFO) and copper-added BFO were synthesized using the coprecipitation method. The incorporation of copper into the BFO lattice led to a reduction in the phase percentage of BFO due to the early formation of $CuBi_2O_4$. X-ray diffraction analysis revealed a decrease in crystallite size up to 0.1 CBFO, followed by an increase. This reduction in crystallite size causes an imbalance between the spins of the sublattices, resulting in an antiferromagnetic core/ferromagnetic shell (AC/FS) structure. The uncompensated spins generated by the decreasing crystallite size weaken the ferromagnetic properties with the addition of Cu. Additionally, the reduction in crystallite size leads to decreased electrical conductivity due to carrier scattering, with the maximum conductivity observed in BFO attributed to its volatilization. The Seebeck coefficient enhancement in 0.1 and 0.15 CBFO indicates an energy filtering effect caused by barriers at the phase boundaries. The introduction of Cu into the BFO matrix also results in reduced lattice thermal conductivity due to active centers for phonon scattering created by Cu-induced defects. The lowest lattice thermal conductivity was observed in 0.1 CBFO, which is attributed to the significant reduction in crystallite size and the presence of phase boundaries enhancing phonon scattering. The highest thermoelectric figure of merit (zT) was achieved in thermally unstable BFO due to Bi^{3+} volatilization, which was mitigated by the formation of $CuBi_2O_4$ in CBFO.

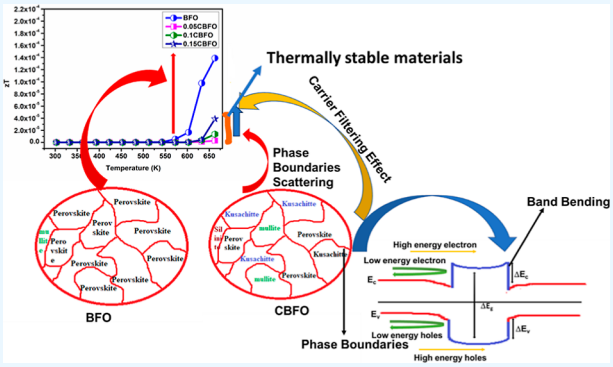

1. INTRODUCTION

Thermoelectric materials help recycle waste heat (generally in the form of heat loss from various processes) from the environment and convert it into electricity. The conversion from waste heat reduces the CO_2 from the atmosphere and helps to keep the earth warm. Today, this importance is raised because of the global boiling effect. The efficiency of this energy conversion is related to the material's intrinsic properties, which are characterized by a dimensionless figure of merit.

$$zT = \frac{S^2\sigma T}{k} \quad (1)$$

where T is the absolute temperature, S is the Seebeck coefficient, σ is the electrical conductivity, and k is the thermal conductivity. An outstanding thermoelectric performance requires a high power factor (PF = $S^2\sigma$) and a low thermal conductivity k.[1]

ABO_3 perovskite exhibits multiferroic properties due to the presence of two or more ferroic orders or coupling between the ferroic orders. Analysis of this property helps determine material suitability for various applications such as sensors, photocatalysis, information storage devices, and optical limiters. $BiFeO_3$, a perovskite which exhibits multiferroic properties by magneto-electric coupling (coupling between two ferroic orders). It shows a ferroelectric transition ~ T_c = 1100 K due to the lone pair of electrons in Bi and G-type antiferromagnetic at Neel temperature ~ T_N = 650 K.[2] Above 386 °C, $BiFeO_3$ has oxygen vacancies due to Bi^{3+} volatilization, and the material shows potential applications in sensors and electronic devices. Thermoelectrical properties of La doped $BiFeO_3$ in mid-temperature ranges are reported. Selected dopant changes the lattice from *R*3*c* to Pbnm, and it increases the material stability by reducing Bi volatilization. $BiFeO_3$ has a maximum figure of merit (zT) of 0.00023 at 703 K due to its high electrical conductivity. However, zT is obtained in the order of 10^{-3}, which is low due to the high thermal conductivity of $BiFeO_3$.[3] As the following studies suggest, Cu has been a suitable dopant to increase the zT by suppressing

Received: June 8, 2024
Revised: July 8, 2024
Accepted: July 11, 2024
Published: July 31, 2024

thermal conductivity. Wang et al. reported that mobile Cu ions suppress the transverse phonon modes, subsequently decreasing thermal conductivity in the superionic phase.[4] Wang et al. reported the enhancement of zT about 4 times by Cu doping into $Bi_2Te_{2.85}Se_{0.1}$. According to this study, the interstitial Cu induces a decrease in carrier concentration and phonon thermal conductivity and an increase in carrier mobility.[5] Deng et al. achieved twice the zT enhancement by suppressing thermal conductivity in Cu-substituted $Ba_8Ga_{16-x}Cu_xSn_{30}$ from 1.25 W/mK (pristine sample) to 0.85 W/mK ($Ba_8Ga_{15.97}Cu_{0.03}Sn_{30}$ sample) at 600 K.[6] Kim et al. reported that the thermal conductivity of Cu-doped samples was reduced as a consequence of an enhanced point defect caused by phonon scattering. The thermal conductivity of the pristine sample was 1.72 W/mK, reduced to 0.93 W/mK for Cu-doped $Bi_2Te_{2.7}Se_{0.3}$. The enhancement of zT by about 92% was obtained via the synergistic effect (the combined effect of power factor and thermal conductivity).[7] Preferably, the above researchers selected divalent Cu as doping into trivalent Ga and Bi. The divalent element was selected as doping into the trivalent site owing to an increase in carrier concentration and induced defects. Increasing carrier concentration increases the electrical conductivity, while the induced defects serve as a scattering center for phonons. Here, we are motivated to dope the Cu^{2+} into Fe^{3+} site to analyze the thermoelectric properties. The coprecipitation method is preferred over ball milling, hydrothermal, solvothermal, and melting[8−10] on account of its several advantages, such as simple and rapid preparation, easy control over particle size and composition, overall homogeneity, low-temperature synthesis, energy efficiency, and no involvement of organic solvents.[10] Based on the above reasons, as mentioned in multiple reports, $BiFeO_3$ was synthesized via the coprecipitation method.[11]

This work aims to synthesize Cu-doped $BiFeO_3$ via a coprecipitation method. Cu presence was identified in the secondary phase in addition to the bismuth ferrite (BFO) phase. The stoichiometric imbalances form the other secondary phases. The phase percentage of $CuBi_2O_4$ was observed to increase with a decreasing BFO phase percentage. The induced strain by decreased lattice parameters caused the average crystallite size to decrease and vice versa. Band bending occurs nearer to the phase boundaries, which helps with carrier filtering with the enhancement of the Seebeck coefficient. BFO has more volatilization of Bi^{3+}, which enhances the electrical conductivity. The Cu addition in BFO diminishes thermal conductivity through the induced compressive strain. Finally, the volatilization of Bi^{3+} helps to obtain the maximum zT for BFO than Cu-added BFO.

2. EXPERIMENTAL SECTION

2.1. Materials and Reagents. $BiFeO_3$ and Cu-added $BiFeO_3$ were synthesized via a coprecipitation method. Analytical-grade reagents: $Bi(NO_3)_3{\cdot}5H_2O$ (99.99%), $Fe(NO_3)_3{\cdot}6H_2O$ (99.99%), $Cu(NO_3)_2{\cdot}6H_2O$ (99.98%), HNO_3, and NaOH were purchased from the Sisco Research Laboratory.

2.2. Synthesis and Characterizations. *2.2.1. Synthesis.* Initially, 0.4 M of HNO_3, which is used as a dissolving agent for $Bi(NO_3)_3{\cdot}5H_2O$, was prepared in a 100 mL standard measuring flask and then transferred to a 1000 mL beaker. Then, 1 mol of $Bi(NO_3)_3{\cdot}5H_2O$ and 1 mol of $Fe(NO_3)_3{\cdot}6H_2O$ were poured into the 1000 mL beaker. For Cu addition, x moles of $Cu(NO_3)_2{\cdot}6H_2O$ (x = 0.05, 0.1, or 0.15) were added to the beaker to replace $Fe(NO_3)_3{\cdot}6H_2O$. The mixture was stirred continuously and added to the same beaker. A brown precipitate was observed when adding NaOH solution, which was further neutralized by adding deionized water and filtering the suspension. After neutralization, the suspension was collected, washed with ethanol, and dried at 110 °C, and the samples were calcined at 600 °C. Fluffy powder was labeled as BFO, 0.05CBFO, 0.1CBFO, and 0.15CBFO. For thermoelectric studies, rectangular pellets (15 mm × 5 mm × 2 mm) and circular pellets (15 mm × 2 mm) were made. Finally, BFO was sintered below at 386 °C, and Cu-added BFO was sintered at 600 °C for 6 h.

2.2.2. Characterizations. The BRUKER USA D8 Advance Davinchi X-ray diffraction (XRD) system was used to analyze crystal structure with the Cu Kα (1.5418 Å) source. The surface morphology of the samples was analyzed by FESEM (Thermo Scientific Apreo S). Raman analysis was performed by back scattering configuration, and an excitation source of wavelength 532 nm was used (HORIBA Scientific with the objective X50_VIS_LWD). The functional group of the sample was analyzed by a Fourier transform infrared spectrometer (Themo Scientific Nicolet iS10). The optical transition was analyzed in the visible region by using a UV−visible spectrophotometer (Thermo Scientific Evolution). The chemical composition on the surface of the samples was analyzed by X-ray photoelectron spectroscopy (XPS) (PHI Versa probe-III). The magnetic properties of synthesized samples were analyzed by vibrating a sample magnetometer with a sensitivity of −11 emu (Lakeshore mini VSM 3639). Hall parameters were measured by using a Hall effect measurement system (Excel Instruments, India). The Seebeck coefficient and electrical conductivity of the samples were measured as a function of temperature ranging from 303 to 663 K (5 °C/min) step size at 30 °C under vacuum conditions by placing the rectangular pellet between the heating and cooling sides (hot stage Seebeck measurement system, Marine, India). The Seebeck coefficient was measured by heating up one side, and the other side is maintained lower than the previous one, resulting in the movement of charge carriers from the hotter to the coder side, which creates the potential difference. The DC four-terminal method was employed to measure the electrical resistance. In this approach, a consistent current (I) was administered to both ends of the sample for assessing and determining the voltage drop (dV) across the thermocouple wires. This involved subtracting the thermoelectromotive force between the leads. Thermal conductivity was measured with the circular geometry of samples by using LFA467 with a step size of 30 °C between 303 and 663 K (NETZSCH, LFA467, Germany). Rietveld refinement was performed by using the Full prof suite software. Lattice parameters, U, V, and W, and the atomic positions of each phase were refined through this software with 20 iterations.

3. RESULTS AND DISCUSSION

The acquired XRD pattern of BFO and Cu-added BFO is shown in Figure 1. The rhombohedral crystal structure of BFO identified with $R3c$ symmetry, and the peak positions were matched with the standard reference JCPDS—72-2035. A similar symmetry was observed in the Ren et al. report.[12] The phase percentages of each individual phase were calculated using the expressions

https://doi.org/10.1021/acsomega.4c05361
ACS Omega 2024, 9, 35088−35099

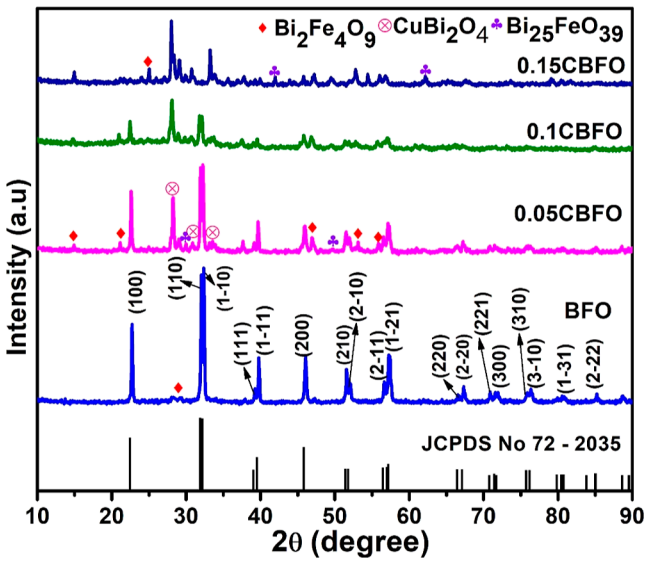

Figure 1. Structural analysis of the synthesized samples.

$$\text{percentage of phase (\%)} = \frac{\text{AUC}_{hkl}}{\sum \text{AUC}_{hkl}} \times 100 \quad (2)$$

Here, AUC_{hkl} is the area under the curve of the peak with the highest intensity of the phase and ΣAUC_{hkl} is the summation of the areas under the curves of the highest intensity peaks of all the phases which were identified in this particular product.[13] Each phase percentage is listed in Table 1. The formation of individual phases is given in eqs 3−12

$$Bi^{3+} + 3OH^- \xrightarrow{RT} Bi(OH)_3 \quad (3)$$

$$Fe^{3+} + 3OH^- \xrightarrow{RT} Fe(OH)_3 \quad (4)$$

$$Cu^{2+} + 2OH^- \xrightarrow{RT} Cu(OH)_2 \quad (5)$$

$$2Bi(OH)_3 \xrightarrow{\Delta+OH^-} Bi_2O_3 + 3H_2O \quad (6)$$

$$2Fe(OH)_3 \xrightarrow{\Delta+OH^-} Fe_2O_3 + 3H_2O \quad (7)$$

$$Cu(OH)_2 \xrightarrow{\Delta+OH^-} CuO + H_2O \quad (8)$$

$$Bi_2O_3 + CuO \xrightarrow{\Delta} CuBi_2O_4 \quad (9)$$

$$Bi_2O_3 + Fe_2O_3 \xrightarrow{\Delta} 2BiFeO_3 \quad (10)$$

$$Bi_2O_3 + 2Fe_2O_3 \xrightarrow{\Delta} Bi_2Fe_4O_9 \quad (11)$$

$$25Bi_2O_3 + Fe_2O_3 \xrightarrow{\Delta} 2Bi_{25}FeO_{39} \quad (12)$$

The equations were taken from a previous reported work.[14,15] The phase diagram of Bi_2O_3−Fe_2O_3 shows that it is not facile to obtain the pure phase of $BiFeO_3$ even with calcination or annealing.[16] After that, as-synthesized BFO contains the secondary phase of $Bi_2Fe_4O_9$.[17] The selected dopant Cu was placed in the $CuBi_2O_4$ phase due to the early formation of this phase with rising temperatures. Usually, the secondary phases of BFO exist in a cocentric spherical model with a rising temperature.[2] Here, the early formation of $CuBi_2O_4$ greatly disturbs the formation of BFO, which leads to a great reduction in the BFO phase percentage in Cu-added BFO. Crystallite size was calculated by Scherrer formulas, and strain was calculated by the Williamson Hall plot. The obtained values clearly indicate a material in which a larger crystallite size has a lower strain value. Compressive strain was induced in the lattice by adding Cu in BFO due to the presence of different densities of each phase, point defects, and dislocations.[18]

Figure 2 shows the Rietveld refinement of BFO and Cu-added BFO. The presence of BFO and the secondary phases are confirmed. As the BFO percentage decreased, Bragg's position of the corresponding phase disappeared. Next, Bragg's position of other phases was matched with the observed peak positions, indicating an increasing other phase percentage due to the Cu addition. Table S1a lists the calculated fitting factors for each phase. Table S1b contains the calculated lattice constant value for each phase in a sample from the refinement. The calculated lattice constant value exactly resembles the trend of calculated crystallite size from the XRD pattern of phases $CuBi_2O_4$ and $BiFeO_3$ by the existing strain. The decreasing lattice constant indicates the compressive strain, while the increasing lattice constant indicates the tensile strain.

BFO and *x*CBFO particles are dispersed on the surface, as shown in Figure 3a−d. Particles resembled irregular nano structures. However, there were no significant changes observed in the particle shape due to the presence of secondary phases. Bernardo et al. showed the formation of BFO by the cocentric model; according to the model, the sequence of Bi_2O_3 diffusion to the particulate core made of Fe_2O_3 forms secondary phases: $Bi_{25}FeO_{39}$/$BiFeO_3$/$Bi_2Fe_4O_9$/Fe_2O_3.[18] A cocentric spherical particle is produced at increasing temperatures for Bi_2O_3 and Fe_2O_3 to form a core of Fe_2O_3 encapsulated by a thin spherical layer of $Bi_2Fe_4O_9$ (mullite). These spherical particles were further encapsulated by a shell thicker than mullite but made of $BiFeO_3$ (perovskite), and the outermost shell was made of $Bi_{25}FeO_{39}$ (sillenite). The outermost shell was determined to be thicker than the mullite layer but thinner than the perovskite, which can be justified by the faster, outward diffusion of Bi_2O_3 than Fe_2O_3. However, this model implies a low percentage of secondary phase formation. Here, the cocentric model collapsed due to the Cu addition into the lattice, and the secondary phases of BFO formed at a very high percentage.

Table 1. Calculated Phase Percentage, Crystallite Size, and Strain Values from XRD Measurements

	phase (%)				*D* (nm)					
sample code	$Bi_2Fe_4O_9$	$CuBi_2O_4$	$Bi_{25}FeO_{39}$	BFO	$Bi_2Fe_4O_9$	$CuBi_2O_4$	$Bi_{25}FeO_{39}$	BFO	D_{avg} (nm)	strain from graph
BFO	1.1			98.9	16.56			38.20	38.2	0.0013
0.05CBFO	16.75	8.65	1	73.6	32.72	37.06	35.96	25.85	32.94	0.0038
0.1CBFO	15.59	26.72	1.08	56.61	43.49	15.79	54.96	18.38	16.28	0.0068
0.15CBFO	23	40	8.38	28.62	28.98	23.03	39.24	30.58	27.43	0.0046

https://doi.org/10.1021/acsomega.4c05361
ACS Omega 2024, 9, 35088−35099

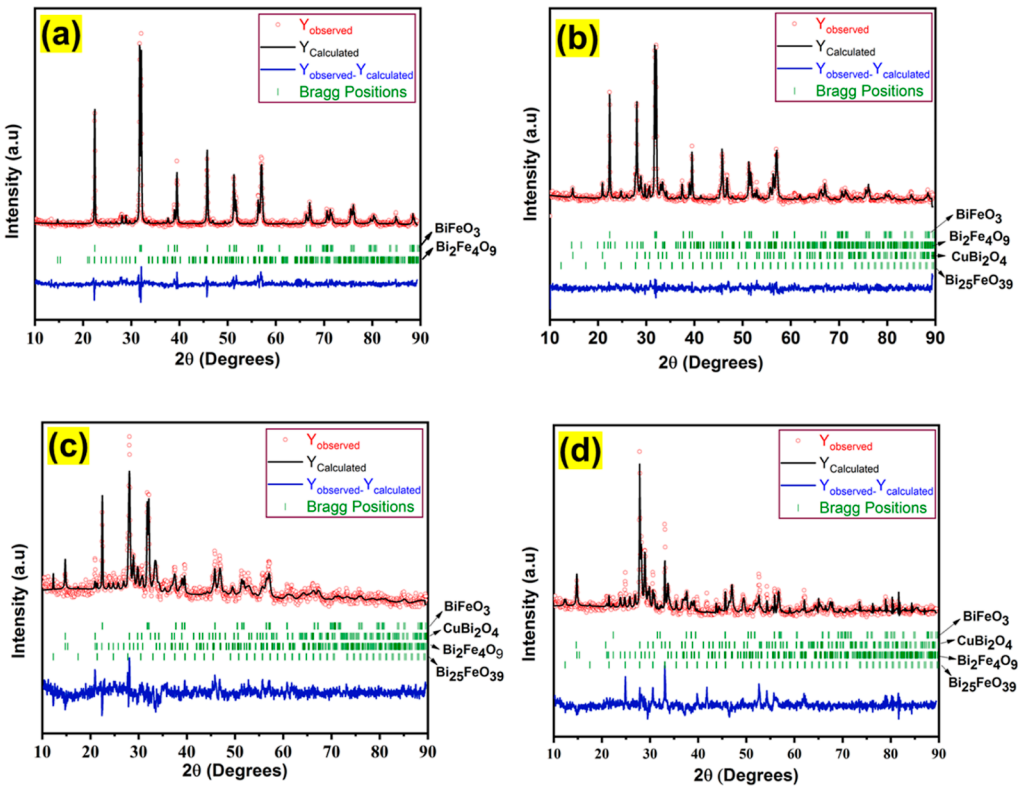

Figure 2. Rietveld refinement for phase analysis: (a) BFO, (b) 0.05CBFO, (c) 0.1CBFO, and (d) 0.15CBFO.

The particle agglomeration seems to be controlled by the added Cu. Figure 3e–f shows the elemental mapping analysis of samples.

The presence of functional groups in synthesized materials and structural information were analyzed via FTIR. Figure 4a shows the FTIR spectra of BFO, 0.05CBFO, 0.1CBFO, and 0.15CBFO between 400 and 2000 cm^{-1}. The peak at 425 and 530 cm^{-1} indicates the stretching vibration of Bi–O.[19] The increasing transmittance percentage of the peak located at 530 cm^{-1} corresponds to a decreasing BFO phase. A peak position at 646 cm^{-1} in 0.05CBFO indicates the Cu–O of $CuBi_2O_4$ phase.[20] It shifts to 667 cm^{-1} in 0.15CBFO due to the lattice strain. Also, the transmittance percentage decreasing represents the increase in Cu–O percentage. Fe–O stretching shows characteristic peaks at 568 cm^{-1}. A peak presence at 811 cm^{-1} indicates the stretching vibrations of Fe–O ions in the FeO_4 tetrahedron, which arise due to $Bi_2Fe_4O_9$,[21] and the decreasing transmittance percentage of this peak was linked to the increasing phase percentage of $Bi_2Fe_4O_9$. The absence of functional groups in the fingerprint region indicates that the materials were free from organic compounds.[22]

Raman spectra results were obtained using a 532 nm wavelength source. Structural details of the obtained spectra are shown in Figure 4b. The reported peak values were matched with the peak values of synthesized materials, which indicates the formation of BFO. Thirteen ($\Gamma = A_1 + 9E$) vibrational modes were listed based on group theory.[23] A_1 modes indicate the movement of bonding with the Bi cation. E modes indicate octahedrally tilted FeO_6 and bond bending.[24] Table S2 shows the vibrational regions in the sample. The presence of $CuBi_2O_4$ was identified from the bonding between Cu and O, which is represented by the peaks at 170.3 and 187.83 cm^{-1} in 0.1CBFO and 0.15CBFO, respectively.[25] This kind of variation was also observed in FTIR. The variations from BFO to xCBFO matrix peak position indicate the changes in bonding between metal cations and anions.

The optical transitions of synthesized materials were analyzed via UV–Vis. BFO has three transitions below 600 nm corresponding to the $BiFeO_3$ phase and two transitions above 600 nm corresponding to $Bi_2Fe_4O_9$. Due to the heterogeneous nature of synthesized materials, small deviations were observed in the absorbance spectrum of Cu-added BFO Figure 5a.

The optical transition was obtained by using Tauc relation

$$(\alpha h\nu)^{(1/n)} = A(h\nu - E_g) \tag{13}$$

where A is the proportionality constant, α is the absorption coefficient, h is Planck's constant, ν is the incident photon frequency, E_g is the band gap, and n is 1/2 for direct band gap or 2 for indirect band gap transition.[26] For direct band gap transitions, the graph plotted for $(\alpha h\nu)^2$ vs incident photon energy $(h\nu)$ is the same as in Figure S1. The nearer transitions of the presented phases make it difficult to predict the band gap accurately for each phase. Thus, the band gap values were calculated using the maximum absorption value. The synthesized BFO sample shows a band gap of 2.13 eV. Then, it decreased as a consequence of decreasing BFO and increasing other phases of Cu-added BFO. As in Table 2, the band gap was found to decrease with decreasing D_{avg} and increase with increasing $D_{avg.}$ The relation to strain band gap decreases with increasing strain and vice versa. The decreasing band gap leads to a narrow band gap semiconducting property that has been ideal for thermoelectric and infrared detectors.

Figure 5b shows the M–H plot of the synthesized materials. Here, a heterogeneous mixture of samples was observed. BFO has weaker ferromagnetic behavior with low M_r and H_c at

https://doi.org/10.1021/acsomega.4c05361
ACS Omega 2024, 9, 35088–35099

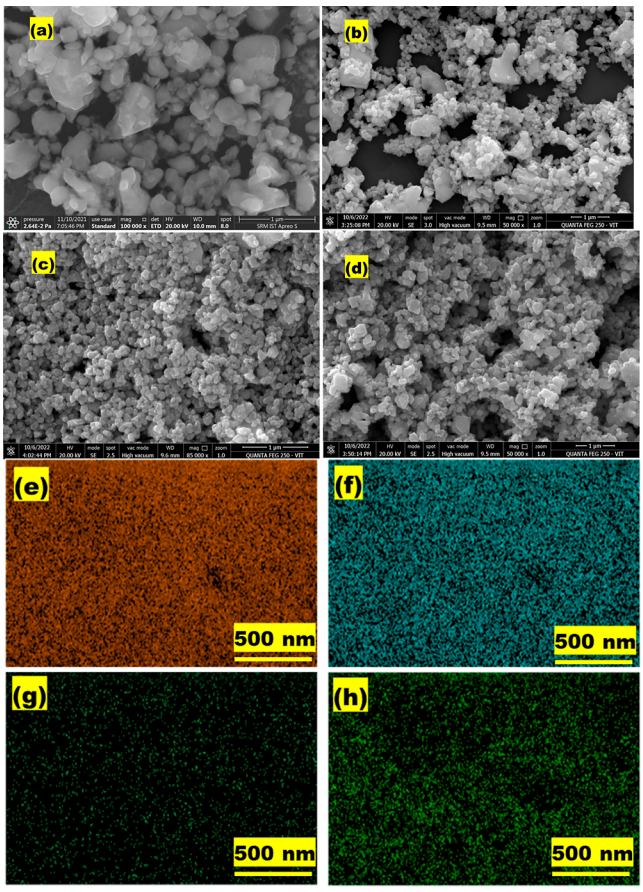

Figure 3. Surface morphology of (a) BFO, (b) 0.05CBFO, (c) 0.1CBFO, and (d) 0.15CBFO; elemental mapping of (e) Bi, (f) Fe, (g) Cu, and (h) O.

room temperature.[27] $CuBi_2O_4$ has a spin 1/2 model compound with ferromagnetically ordered chains that are antiferromagnetically arranged with respect to each other. $Bi_{25}FeO_{39}$ selenite has ferromagnetic behavior.[28] Q. Zhang et al. discussed the magnetic properties of $Bi_2Fe_4O_9$ upon size reduction effect as below. According to those explanations, the antiferromagnetic nature of mullite is exhibited in two antiparallel spin sublattices. The spins are aligned parallelly in each sublattice, while the spins are aligned antiparallelly between two sublattices. The reducing crystallite size causes the spins of one sublattice to not be compensated by another sublattice, resulting in an antiferromagnetic core (AC)/ferromagnetic shell (FS) structure. This mechanism creates a number of uncompensated spins with decreasing crystallite size.[29] From these results, we infer that the grain size: 42−14 nm has a weaker ferromagnetic section. $Bi_2Fe_4O_9$ deviates from an antiferromagnetic to a weaker ferromagnetic nature upon size reduction by increasing the number of uncompensated spins with decreasing crystallite size. Our experimental results showed the magnetic influence of $Bi_2Fe_4O_9$ to be more in the Cu-added BFO with a size less than 43 nm. The contribution of $Bi_2Fe_4O_9$ prompts the material to possess ferromagnetic properties due to the size effect. As a net influence of phases, the whole sample possesses ferromagnetic behavior, which is weaker. Upon size reduction, the coercive field decreases.[30] The increase in other phases such as $CuBi_2O_4$, $Bi_{25}FeO_{39}$, and $Bi_2Fe_4O_9$ in the sample affects the ferromagnetic nature, making it weaker by increasing the number of uncompensated spins because M_r was gradually decreasing with increasing Cu addition, as shown in Figure 5c. Table 3 contains the various values of H_c, M_r, and M_s.

The surface composition of synthesized 0.05CBFO was analyzed. Figure 6a shows the survey spectrum of 0.05CBFO and reveals the presence of Bi, Cu, Fe, and O. Figure 6b shows the spectrum of Bi elements, which has split states of $4f_{7/2}$ and $4f_{5/2}$. The binding energy of peaks indicates the presence of cationic Bi^{3+}. The peaks $4f_{7/2}$ and $4f_{5/2}$ are located at 158.76 and 164.06 eV, respectively. It indicates that all phases contain Bi^{3+}.[31] Figure 6c shows the spin orbit splitting states of Cu are $2p_{3/2}$ and $2p_{1/2}$. The peak position indicates the valence states of 2+ and 1+. The binding energies of Cu^{2+} are 934.64 and 954.16 eV for $2p_{3/2}$ and $2p_{1/2}$, respectively. The binding energies of Cu^{1+} are 933.16 and 954.16 eV for $2p_{3/2}$ and $2p_{1/2}$, respectively. The ratio of Cu^{2+}:Cu^{1+} is 0.80:0.20, which indicates that Cu is present with more Cu^{2+}. Cu has a 2+ oxidation state in $CuBi_2O_4$, which indicates A^{2+} $B_2^{3+}O_4^{2-}$. Figure 6d shows a spectrum of Fe. Fe spin orbit splitting states are Fe $2p_{3/2}$ and Fe $2p_{1/2}$. The peak positions indicate the presence of Fe^{3+}. The peaks $2p_{3/2}$ and $2p_{1/2}$ are located at different positions of 710.5 and 724.36 eV, respectively.[32] The peak around 715.08 indicates Fe^{3+} multiple splitting and electron shake-up. The peak of Fe $2p_{3/2}$ could be divided into

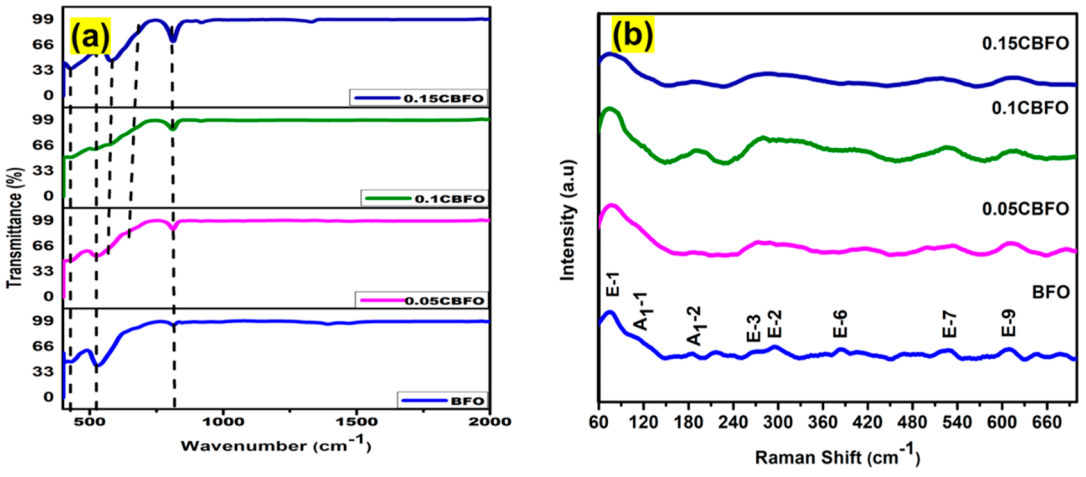

Figure 4. (a) Functional group analysis of synthesized samples and (b) vibrational modes of BFO, 0.05CBFO, 0.1CBFO, and 0.15CBFO.

https://doi.org/10.1021/acsomega.4c05361
ACS Omega 2024, 9, 35088−35099

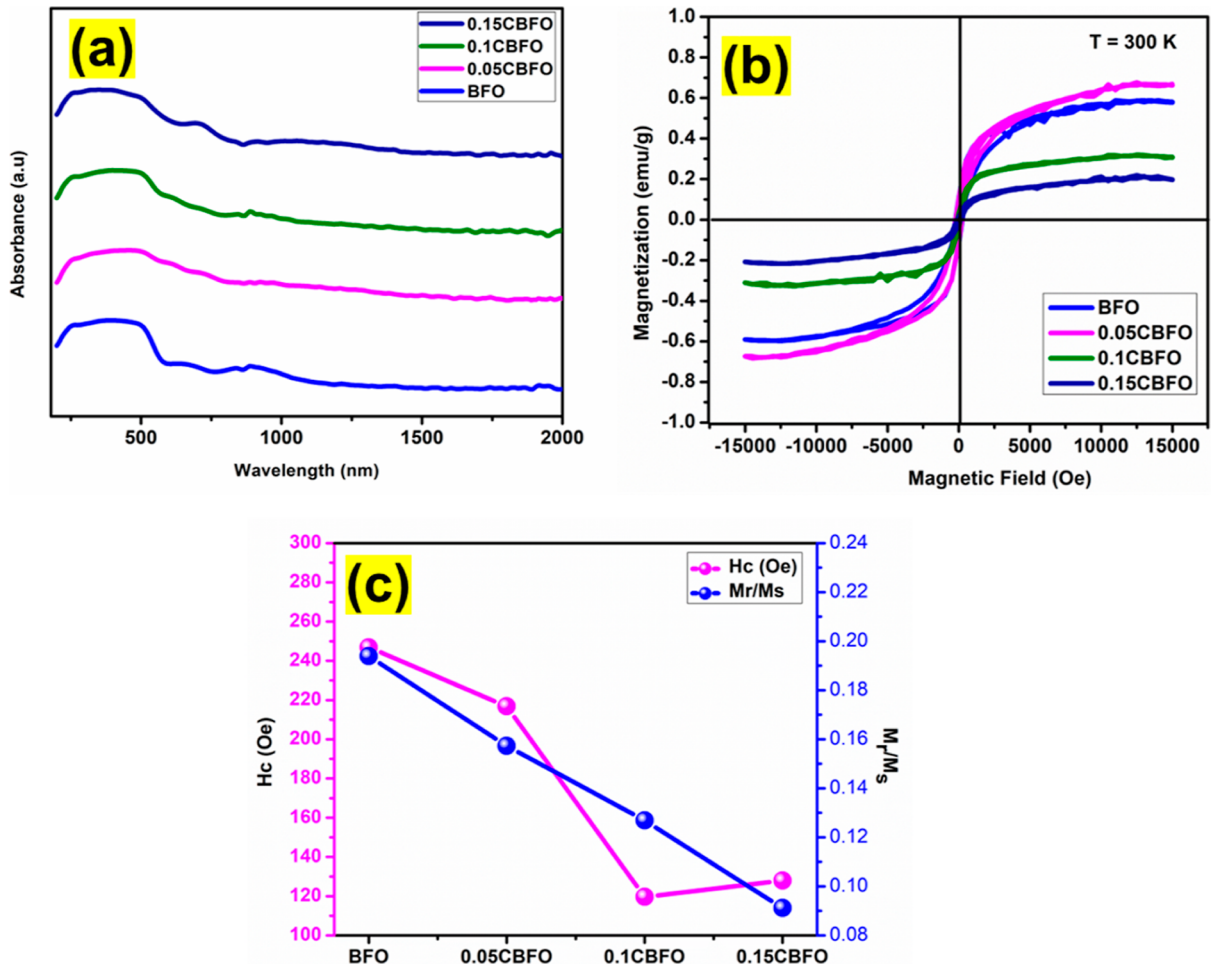

Figure 5. BFO and Cu-added BFO (a) optical absorption spectrum, (b) band gap analysis from the Tauc plot, and (c) weak ferromagnetic nature of the M−H loop at various H_c and M_r/M_s values.

Table 2. Variation of the Band Gap with Crystallite Size

material	band gap (eV)	D_{avg} (nm)	Strain
BFO	2.13	38.2	0.0013
0.05CBFO	1.83	32.94	0.0038
0.1CBFO	1.60	16.28	0.0068
0.15CBFO	1.80	27.43	0.0046

Table 3. Parameters Were Calculated from VSM Analysis

material	H_c	M_s	M_r	M_r/M_s
BFO	246.87	0.593	0.115	0.1939
0.05CBFO	216.83	0.680	0.107	0.1573
0.1CBFO	119.65	0.323	0.041	0.1269
0.15CBFO	127.97	0.218	0.020	0.0917

three peaks at binding energies of 712.87, 711.26, and 710.43 eV, respectively. These three peaks indicated the presence of the Fe−O bond in different compositions. Figure 6e shows a spectrum of O 1s where three different characteristics of O 1s were observed.[33] The presence of lattice oxygen vacancies can be explained by the intense peak, which confirms the presence of more dangling bond oxygens. This behavior is used for sensing applications.

Carrier concentration and hall mobility were calculated by hall measurements. Figure 7 portrays hall measurements of the materials. All materials have carrier concentrations on the order of 10^{15}−10^{17} cm^{-3}, where they increase with increasing dopant concentration. BFO has a value of 3.22×10^{15} cm^{-3}. The negative sign of carrier concentration indicates the n-type transport behavior of 0.1CBFO and 0.15CBFO. The hall mobility of the materials was found to be maximum when the material had a minimum carrier concentration. A maximum hall mobility of 39.02 $cm^2\ V^{-1}\ s^{-1}$ was obtained for 0.15CBFO.

The electrical transport properties as a function of temperature for all samples are shown in Figure 8. Electrical conductivity increases as a function of temperature, as shown in Figure 8a. The nature of the curve reveals the two characteristics of transport. Electrical transport was contributed by charge carriers from 303 to 513 K. After that, the gradual increasing trend confirms the contribution of ions in transport. BFO exhibits a higher electrical conductivity of 10.2 S m^{-1} at 663 K than Cu-added BFO because the oxygen vacancies created by the volatilization of Bi^{3+} tend to create ions. Later, it was tailored to fluctuate from Fe^{3+} to Fe^{2+}.[34] The conductivity decreased on increasing the phase percentage of $CuBi_2O_4$ while decreasing the phase percentage of BFO. Suppression of ionic conductivity was confirmed by a decrement of conductivity from BFO about 143.6, 1052, and 1020 times at 663 K for 0.05CBFO, 0.1CBFO, and 0.15CBFO, respectively. This sizable reduction is influenced by the carrier filtering effect at phase boundaries. The impact of crystallite size on σ is observed by a phase-boundary scattering

https://doi.org/10.1021/acsomega.4c05361
ACS Omega 2024, 9, 35088−35099

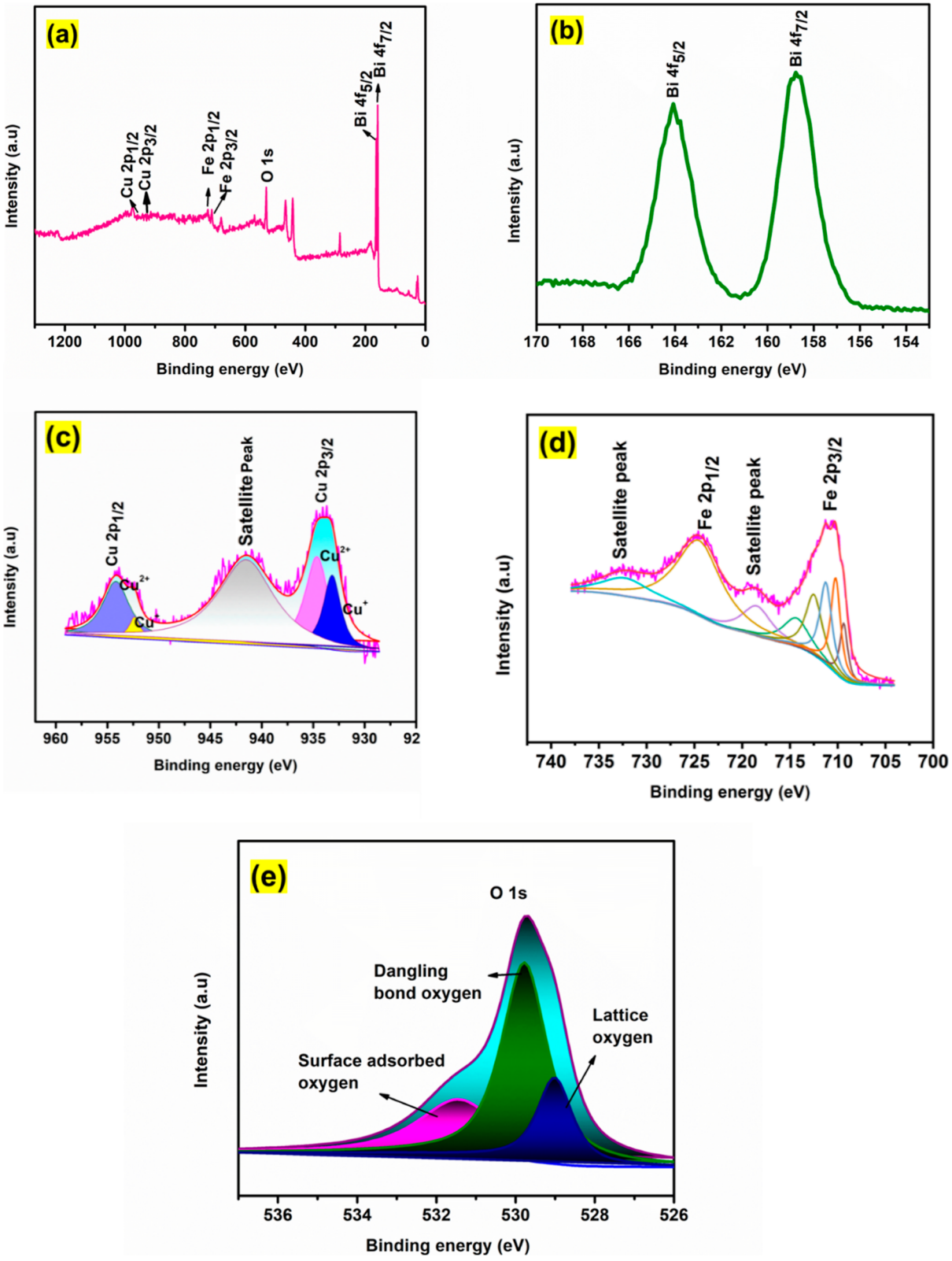

Figure 6. Compositional analysis: (a) survey spectrum, (b) Bi 4f, (c) Fe 2p, (d) Cu 2p, and (e) O 1s.

mechanism. The scattering effect of charge carries further reduces the σ from 0.05CBFO than that of BFO. Any material with a larger crystallite size has reduced the scattering of charge carriers on the boundaries, which leads to increased σ.[35] The relation between crystallite size and σ is shown in Figure 8b.

Arrhenius plots of the synthesized material are shown in Figure 8c. The material has two distinct regional transports, as discussed in σ. In the low-temperature region, where the conduction is dominated by carriers, the slope is nearly constant, and in the high-temperature region, where it is dominated by ions, the slope is higher than at low

https://doi.org/10.1021/acsomega.4c05361
ACS Omega 2024, 9, 35088−35099

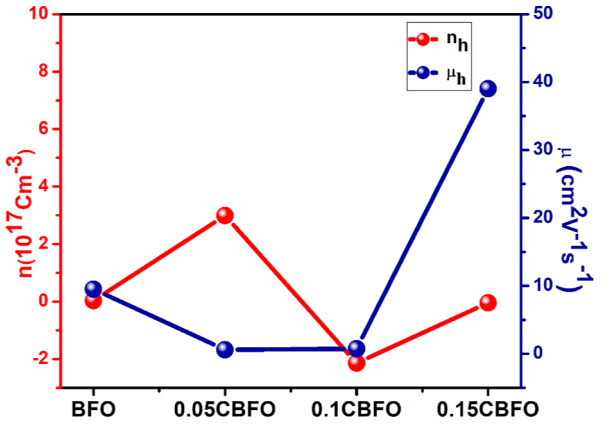

Figure 7. Carrier concentration and mobility values at room temperature for BFO, 0.05CBFO, 0.1CBFO, and 0.15CBFO.

temperatures. The calculated activation energy decreases upon increasing $CuBi_2O_4$ phase, as listed in Table 4. The calculated activation energy of materials in the rising region indicate the oxide ion conduction in BFO and 0.05CBFO, as discussed by Li et al.[36] However, the ionic conductivity behavior is suppressed upon increasing $CuBi_2O_4$ phase in 0.1CBFO and 0.15CBFO.

The Seebeck coefficient of materials increases with increasing temperature, as shown in Figure 8d. Majority carriers in a material were identified from the majority carriers in each phase. BFO and 0.05CBFO have a positive value of Seebeck coefficient due to the majority carries as holes, which contain maximum BFO and minimum $CuBi_2O_4$. 0.1CBFO and 0.15CBFO show fluctuations between p-type and n-type where transport could be dominated by carriers. In the ionic conduction region, the fluctuations fade out and the negative ions dominate, allowing it to cross the barrier easily. After that, the energy filtering effect was observed in 0.15CBFO from observed mobility, multiple phase formation, and the Seebeck coefficient. According to the Bethe-Sommerfeld expansion (eq 14)

$$S = \frac{\pi k_B^2 T}{3q}\left[\frac{\mathrm{d}n(E)}{n\mathrm{d}E} + \frac{1}{\mu}\frac{\mathrm{d}\mu(E)}{\mathrm{d}E}\right]\mathrm{at} \qquad E = E_f \tag{14}$$

where q is the carrier charge, E is the energy, $\mu(E)$ is the carrier mobility ($\mu = q\ \tau/m^*$), $n(E)$ and $\mu(E)$ are the energy-dependent density of states and mobility, k_B is the Boltzmann constant, m^* is the effective mass, and E_f is the Fermi energy. Mathematically, the second part $\frac{\mathrm{d}\mu(E)}{\mathrm{d}E}$ relates with the S through energy filtering effect. Experimentally, the large mobility evidence for enhancement in S values.[37] The same trend was observed in 0.15CBFO.S is related to the energy derivative of the electronic density of states $n(E)$ and the relaxation time $\tau(E)$ through Mott's relation.[38] Besides, the energy dependence of relaxation time $\tau(E)$ strongly varies with band bending at phase boundaries, which helps to enhance S by filtering low energy carriers and ions. Evidence of this mechanism was observed in the increasing phase percentage of $CuBi_2O_4$ phases upon decreasing BFO. The literature studies indicate that the majority of phases observed, such as $Bi_2Fe_4O_9$ and $CuBi_2O_4$, have a smaller band gap than BFO, which helps in band bending at phase boundaries due to the mismatching of the band gap values. Here, heterogeneous composition, such as $Bi_2Fe_4O_9$ and $CuBi_2O_4$, along with BFO in high percentage, bend the bands at phase boundaries, which leads to barrier formation and the low energy carriers being filtered out by an energy filtering mechanism. Followed by the high-energy carriers, crossing the boundaries effectively increases the Seebeck coefficient values, as illustrated in Figure 8e. From this mechanism, the S values of 0.1CBFO and 0.15CBFO were increased, which led to a large enhancement of the S value in 0.15CBFO and the maximum Seebeck coefficient of −1001.9 μV K^{-1} obtained at 663 K.

Weighted mobility was calculated with the combined effect of electrical conductivity and Seebeck coefficient at 303 K, as shown in Figure 8f. Due to the high value of electrical conductivity, BFO has higher weighted mobility than Cu-added BFO. Further carrier filtering effect reduces the weighted mobility of other synthesized materials. The power factor of synthesized materials increases with increasing temperature, as shown in Figure 8g. BFO has a maximum power factor of 0.0783 μW m^{-1} K^{-2} at 663 K. A maximum power factor of 0.0106 μW m^{-1} K^{-2} was observed for 0.15CBFO at 663 K among Cu-added BFO. Unfortunately, a great reduction was seen even with the presence of carrier filtering, and the decreased crystallite size was found to be ineffective in obtaining a maximum power factor than BFO. The calculated parameters related to the power factor are given in Table 5.

The thermal conductivity of the BFO and Cu-added BFO matrix was calculated by $\kappa = \rho C_p D_p$, where ρ is the density of material, C_p is the specific heat capacity, and D_p is the thermal diffusivity.[39] The calculated diffusivities of BFO and Cu-added BFO matrix are shown in Figure 9a. The diffusivity of materials decreases favorably from room temperature to 663 K. The minimum diffusivity of 0.229 mm^2/s was obtained for 0.1CBFO at 663 K. The heat capacity of the Cu-added BFO matrix decreased, but this was oppositely oriented toward the BFO material, as shown in Figure 9b. A minimum heat capacity of 0.472 J Kg^{-1} K^{-1} was obtained for 0.15CBFO at 663 K. κ_t decreases monotonically with increasing temperature, as shown in Figure 9c. κ_t of samples decreased in the order BFO > 0.05CBFO > 0.15CBFO > 0.1CBFO at 663 K. The order reveals κ_t was low in Cu-added BFO, which indicates interstitially placed Cu or substituted Cu on Bi vacancies in $CuBi_2O_4$ acting as phonon scattering centers. The calculated thermal conductivity of 0.1CBFO was minimum, which shows minimal thermal diffusivity and minimal heat capacity in comparison to other samples at different temperatures. The minimum κ_t of 0.666 W m^{-1} K^{-1} was calculated for 0.1CBFO at 663 K, which was the lowest of all the samples. κ_t also intrinsically depends on κ_e and κ_l. κ_e describes thermal conductivity due to carrier transport calculated from Weidmann Franz law $\kappa_e = L\sigma T$.[40] Materials have negligible κ_e due to less electrical conductivity and low value of Lorentz number. Due to the negligible value of κ_e, the value was not calculated separately, and κ_t is fully described by κ_l. κ_l describes the thermal conduction due to lattice phonons calculated by $\kappa_l = \kappa_t - \kappa_e$. The strain due to the presence of heterogeneous phases possibly may have reduced the crystallite size by dislocations and point defects, which is efficient for scattering. The strain in the order of BFO < 0.05CBFO < 0.15CBFO < 0.1CBFO is oppositely oriented with κ_l. Long-range phonon scattering on phase boundaries increases with decreasing crystallite size, which causes a decrease in thermal conductivity. However, short-range phonons scatter on created point defects due to oxygen vacancies and the position of interstitial or

https://doi.org/10.1021/acsomega.4c05361
ACS Omega 2024, 9, 35088−35099

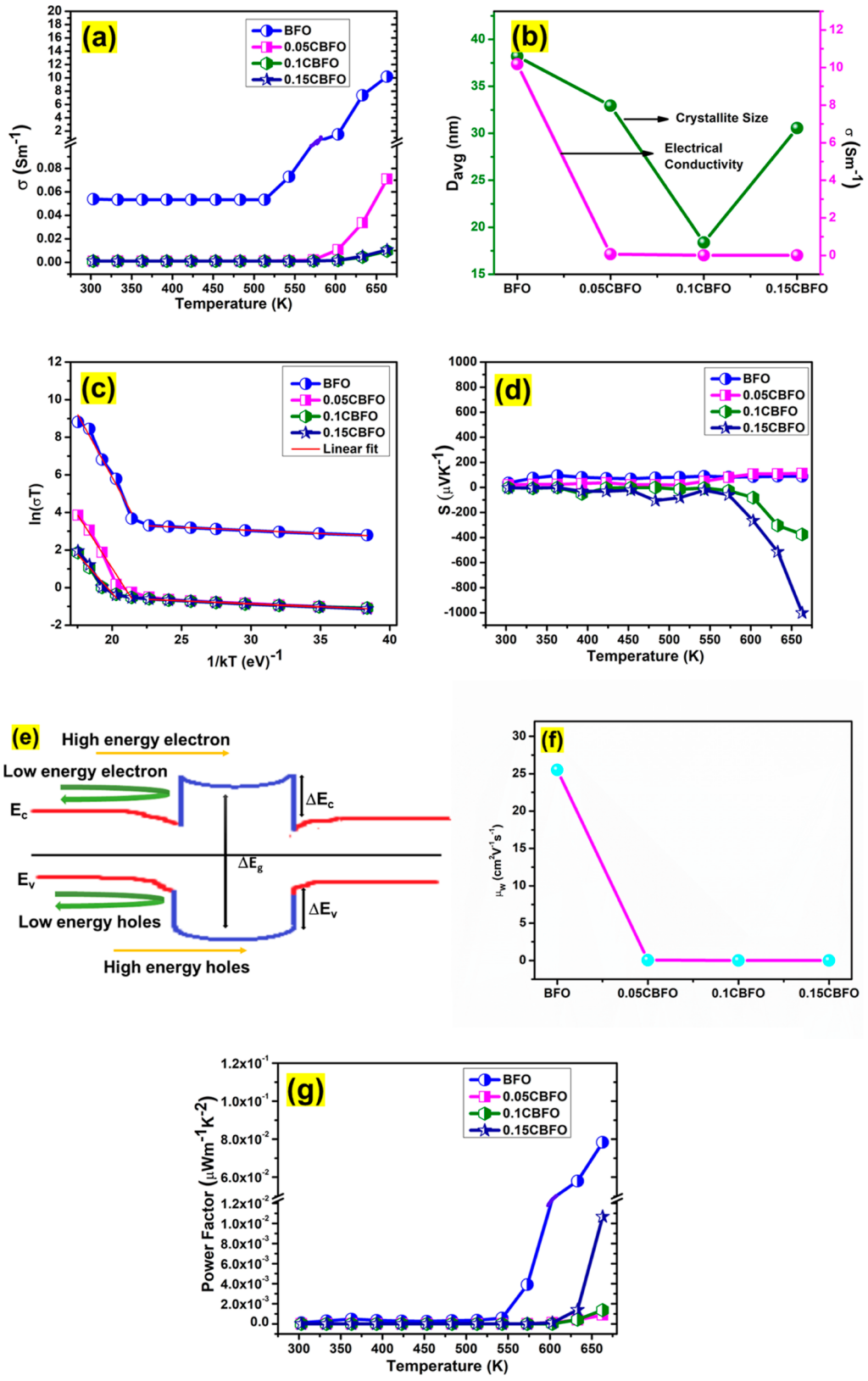

Figure 8. BFO and *x*CBFO carrier transport with temperatures ranging from 303 to 663 K (a) electrical conductivity, (b) D_{avg} vs σ, (c) linear and rising region of Arrhenius plot (d) *S*, (e) illustration of band bending at phase boundaries, (f) weighted mobility, and (g) power factor.

substitutional Cu. The maximum reduction of crystallite size in 0.1CBFO highly suppresses the lattice thermal conductivity, which is revealed in κ_t.

The zT of the material increases with increasing temperature, as shown in Figure 9d. The maximum zT of 1.39×10^{-5} calculated for BFO at 663 K due to high electrical conductivity results from the volatilization of Bi^{3+}, which leads to a thermal

https://doi.org/10.1021/acsomega.4c05361
ACS Omega 2024, 9, 35088−35099

Table 4. Calculated Activation Energy of Materials in Different Regions

material	region	R^2	E_a (eV)
BFO	linear region	0.99	0.034
	rising region	0.96	1.34
0.05CBFO	linear region	0.96	0.035
	rising region	0.96	1.14
0.1CBFO	linear region	0.97	0.031
	rising region	0.94	0.83
0.15LBFO	linear region	0.99	0.033
	rising region	0.96	0.668

Table 5. Calculated Parameters in Maximum Values at a Given Temperature

material	σ (S m^{-1}) at 663 K	S (μV K^{-1}) at 663 K	power factor (μW m^{-1} K^{-2}) at 663 K
BFO	10.2	87.703	0.0783
0.05CBFO	7×10^{-2}	111.5	0.0008
0.1CBFO	9.7×10^{-3}	−375.5	0.0013
0.15CBFO	1.06×10^{-2}	−1001.9	0.0106

instability after 659 K. Cu-added BFO has a lower zT than BFO, and the maximum zT of 0.389×10^{-5} was observed for 0.15 CBFO at 663 K among Cu-added BFO. The increment percentage of zT in 0.15CBFO is about 1330% higher than in 0.05CBFO where the power factor increment was 820% due to phase boundary scattering and crystallite size reduction.

4. CONCLUSIONS

BFO and Cu-added BFO were synthesized via a coprecipitation method. Added Cu as a dopant forms the $CuBi_2O_4$ phase due to the early crystallization of this compound, while the BFO phase percentage was decreased. The decreasing crystallite size increases the strain value on the lattice until 0.1CBFO. Besides, increased strain decreases the band gap and vice versa. Irregular-shaped nanoobjects were observed on the surface of the FESEM image. The presence of all elements such as Bi, Cu, Fe, and O was confirmed through XPS. Decreasing M_r from BFO indicates a further increase in weak ferromagnetic nature by the formation of AC/FS with decreasing crystallite size. The coercive field was observed to decrease with decreasing crystallite size. Due to more volatilization of Bi^{3+} in BFO, the σ of 10.2 Sm^{-1} was higher than Cu-added BFO. The energy filtering effect was observed on increasing the $CuBi_2O_4$ phase, which shows increments in the Seebeck coefficient. A maximum power factor of 0.0783 μW m^{-1} K^{-2} was obtained for BFO where the maximum σ was at 663 K. A minimum thermal conductivity of 0.666 W m^{-1} K^{-1} was obtained in the low crystallite size and the highly strained 0.1CBFO lattice. These features helped scatter a greater number of long-range phonons. However, other Cu-added BFO has minimum thermal conductivity due to the defects created by Cu. The maximum zT obtained for BFO was found to be greater than that of Cu-added BFO. The carrier filtering effect from phase boundaries and phonon

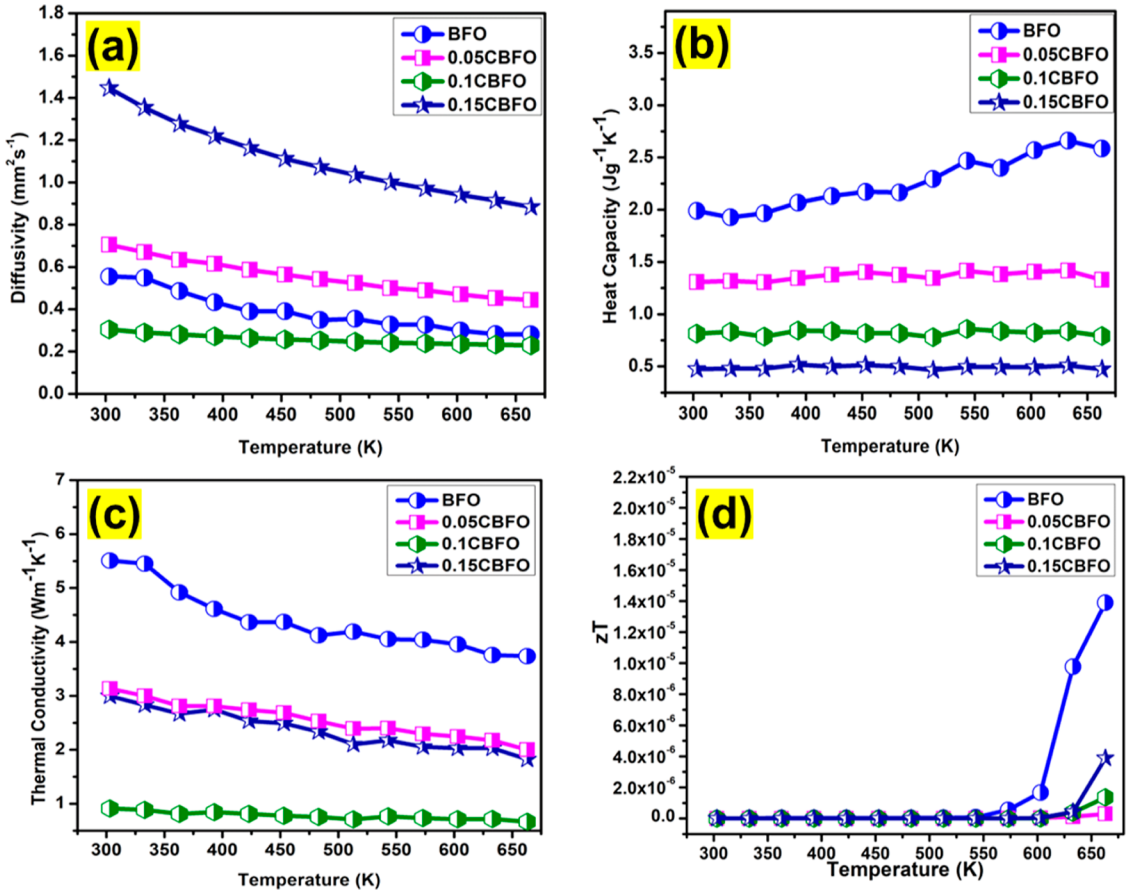

Figure 9. BFO and CBFO measurements as a function of temperature from 303 to 663 K (a) diffusivity, (b) heat capacity, (c) thermal conductivity, and (d) zT.

https://doi.org/10.1021/acsomega.4c05361
ACS Omega 2024, 9, 35088−35099

scattering on decreasing crystallite possesses the maximum zT for 0.15C BFO at 663 K.

■ ASSOCIATED CONTENT

Supporting Information

The Supporting Information is available free of charge at https://pubs.acs.org/doi/10.1021/acsomega.4c05361.

Rietveld fitting profile factors value for each phase; lattice constant value before and after refinement for each phase; Raman peaks comparison; and band gap values obtained from the Tauc plot of synthesized materials (PDF)

■ AUTHOR INFORMATION

Corresponding Author

Navamathavan Rangaswamy − *Department of Physics, School of Advanced Sciences, Vellore Institute of Technology (VIT) Chennai, Chennai 600127, India;* orcid.org/0000-0002-9185-6837; Email: navamathavan.r@vit.ac.in, navmath@yahoo.com

Authors

Krishnamoorthy Aishwarya − *Department of Physics, School of Advanced Sciences, Vellore Institute of Technology (VIT) Chennai, Chennai 600127, India*

Selvam Maruthasalamoorthy − *Department of Physics, School of Advanced Sciences, Vellore Institute of Technology (VIT) Chennai, Chennai 600127, India*

Ramalingam Thenmozhi − *Department of Physics, School of Advanced Sciences, Vellore Institute of Technology (VIT) Chennai, Chennai 600127, India*

Jayaraman Mani − *Department of Nuclear Physics, University of Madras, Chennai 600025, India;* orcid.org/0000-0001-7030-1771

Gopalakrishnan Anbalagan − *Department of Physics, Presidency College, Chennai 600005, India;* Present Address: Department of Nuclear Physics, University of Madras, Chennai—600025, India)

Rajkumar Nirmala − *Department of Biotechnology, Hindustan College of Arts and Science, Affiliated to University of Madras, Chennai 603103, India*

Mani Navaneethan − *Functional Materials and Energy Devices Laboratory, Department of Physics and Nanotechnology, SRM Institute of Science and Technology, Kattankulathur 603203, India; Nanotechnology Research Centre (NRC), Faculty of Engineering and Technology, SRM Institute of Science and Technology, Kattankulathur 603203, India*

Complete contact information is available at: https://pubs.acs.org/10.1021/acsomega.4c05361

Notes

The authors declare no competing financial interest.

■ ACKNOWLEDGMENTS

The authors thank the VIT for providing "VIT RGEMS SEED GRANT" for carrying out this research work. The research was also supported by the UGC-DAE Consortium for Scientific Research under the CSR Project (ref.: CRS/2021-22/04/610).

■ REFERENCES

(1) Wu, Y.; Lou, Q.; Qiu, Y.; Guo, J.; Mei, Z. Y.; Xu, X.; Feng, J.; He, J.; Ge, Z. H. Highly Enhanced Thermoelectric Properties of Nanostructured Bi_2S_3 Bulk Materials: Via Carrier Modification and Multi-Scale Phonon Scattering. *Inorg. Chem. Front.* **2019**, *6* (6), 1374−1381.

(2) Parwin, S.; Parui, J. Time-Temperature-Transformation of $BiFeO_3$ Phase Synthesized by Citrate-Nitrate Route and a Synergetic Effect for Its Stabilization. *J. Chem. Thermodyn.* **2021**, *156* (3), 106347.

(3) Aishwarya, K.; Navamathavan, R. Effect of Grain Size and Orthorhombic Phase of La Doped $BiFeO_3$ on Thermoelectric Properties. *J. Alloys Compd.* **2023**, *947*, 169452.

(4) Wang, B.; Xiang, H.; Nakayama, T.; Zhou, J.; Li, B. Theoretical Investigation on Thermoelectric Properties of Cu-Based Chalcopyrite Compounds. *Phys. Rev. B* **2017**, *95*, 035201.

(5) Wang, Z. L.; Onda, T.; Chen, Z. C. Effect of Cu Doping on Microstructure and Thermoelectric Properties of $Bi_2Te_{2.85}Se_{0.15}$ Bulk Materials. *Scr. Mater.* **2018**, *146*, 119−122.

(6) Deng, S.; Be, M.; In, I. High Thermoelectric Performance of Cu Substituted Type-VIII Clathrate $Ba_8Ga_{16-X}Cu_xSn_{30}$. *J. Appl. Phys.* **2011**, *109*, 103704.

(7) Kim, G.; Lee, K.; Shin, H.; Kim, J.; Chang, J.; Roh, J. W.; Lee, W. Strong Enhancement of Room-Temperature Thermoelectric Properties of Cu-Doped $Bi_2Te_{2.7}Se_{0.3}$. *Appl. Phys. Lett.* **2022**, *120*, 043903.

(8) Liu, N.; Jensen, W. A.; Zebarjadi, M.; Floro, J. A. Tunable β-$FeSi_2$ - $Si_{1-y}Ge_y$ Nanocomposites by a Novel React/Transform Spark Plasma Sintering Approach for Thermoelectric Applications. *Mater. Today Phys.* **2018**, *4*, 19−27.

(9) Pei, Y.; Heinz, N. A.; Snyder, G. J. Alloying to Increase the Band Gap for Improving Thermoelectric Properties of Ag_2Te. *J. Mater. Chem.* **2011**, *21* (45), 18256−18260.

(10) Karpinsky, D. V.; Troyanchuk, I. O.; Tovar, M.; Sikolenko, V.; Efimov, V.; Kholkin, A. L. Evolution of Crystal Structure and Ferroic Properties of La-Doped $BiFeO_3$ Ceramics near the Rhombohedral-Orthorhombic Phase Boundary. *J. Alloys Compd.* **2013**, *555*, 101−107.

(11) Aishwarya, K.; I, H. J.; Maruthasalamoorthy, S.; Nirmala, R.; Punithavelan, N.; Navamathavan, R. Review—State of the Art of the Multifunctional Bismuth Ferrite: Synthesis Method and Applications. *ECS J. Solid State Sci. Technol.* **2022**, *11* (4), 43010.

(12) Ren, X.; Fan, H.; Zhao, Y.; Liu, Z. Flexible Lead-Free $BiFeO_3$/PDMS-Based Nanogenerator as Piezoelectric Energy Harvester. *ACS Appl. Mater. Interfaces* **2016**, *8*, 26190−26197.

(13) Aishwarya, K.; Maruthasalamoorthy, S.; Mani, J.; Anbalagan, G.; Nirmala, R.; Navaneethan, M.; Navamathavan, R. Structural Formation of Multifunctional $NiMoO_4$ Nanorods for Thermoelectric Applications. *Phys. Chem. Chem. Phys.* **2022**, *24* (41), 25620−25629.

(14) Hu, Z. T.; Chenb, B.; Lim, T. T. Single-Crystalline $Bi_2Fe_4O_9$ Synthesized by Low- Temperature Co-Precipitation: Performance as Photo- and Fenton Catalysts. *RSC Adv.* **2014**, *4*, 27820−27829.

(15) Abdulkarem, A. M.; Li, J.; Aref, A. A.; Ren, L.; Elssfah, E. M.; Wang, H.; Ge, Y.; Yu, Y. $CuBi_2O_4$ Single Crystal Nanorods Prepared by Hydrothermal Method: Growth Mechanism and Optical Properties. *Mater. Res. Bull.* **2011**, *46* (9), 1443−1450.

(16) Zhang, T.; Shen, Y.; Qiu, Y.; Liu, Y.; Xiong, R.; Shi, J.; Wei, J. Facial Synthesis and Photoreaction Mechanism of $BiFeO_3/Bi_2Fe_4O_9$ Heterojunction Nano Fi Bers. **2017**, *5*, 4630−4636. .

(17) Taazayet, W. B.; Zouari, I. M.; Mliki, N. T.; Dkhil, B.; Mliki, N. T. Facile Synthesis of Pure $BiFeO_3$ and Bi_2Fe_4 O_9 Nanostructures with Enhanced Photocatalytic Activity. *J. Mater. Sci. Mater. Electron.* **2022**, *33* (5), 2518−2533.

(18) Bernardo, M. S.; Jardiel, T.; Peiteado, M.; Caballero, A. C.; Villegas, M. Reaction pathways in the solid state synthesis of multiferroic $BiFeO_3$. *Journal of the European Ceramic Society* **2011**, *31* (16), 3047−3053.

(19) Rubavathi, P. E.; Benoy, S. M.; Baskar, K.; Venkidu, L.; Babu, M. V. G.; Dhayanithi, D.; Giridharan, N. V.; Sundarakannan, B. Impact of Non-Magnetic $BaTiO_3$ Substitution on Structure, Magnetic, Thermal and Ferroelectric Properties of $BiFeO_3$ Ceramics at

Morphotropic Phase Boundary. *Mater. Chem. Phys.* **2020**, *255* (February), 123560.
(20) Yuvaraj, S.; Karthikeyan, K.; Kalpana, D.; Lee, Y. S.; Selvan, R. K. Surfactant-Free Hydrothermal Synthesis of Hierarchically Structured Spherical $CuBi_2O_4$ as Negative Electrodes for Li-Ion Hybrid Capacitors. *J. Colloid Interface Sci.* **2016**, *469*, 47−56.
(21) Zhao, S.; Wang, G.; Zheng, R.; Liu, Y. Influence of Parasitic Phases on the Magnetic Properties of $BiFeO_3$ Powders. *IOP Conf. Ser. Mater. Sci. Eng.* **2019**, *612* (2), 022035.
(22) Abushad, M.; Khan, W.; Naseem, S.; Husain, S.; Nadeem, M.; Ansari, A. Influence of Mn Doping on Microstructure, Optical, Dielectric and Magnetic Properties of $BiFeO_3$ Nanoceramics Synthesized via Sol-Gel Method. *Ceram. Int.* **2019**, *45* (6), 7437−7445.
(23) Guo, R.; Fang, L.; Dong, W.; Zheng, F.; Shen, M. Enhanced Photocatalytic Activity and Ferromagnetism in Gd Doped $BiFeO_3$ Nanoparticles. **2010**, *114*, 21390-21396. .
(24) Sahni, M.; Mukhopadhyay, S.; Mehra, R. M.; Chauhan, S.; Chandra Sati, P.; Kumar, M.; Singh, M.; Kumar, N. Effect of Yb/Co Co-Dopants on Surface Chemical Bonding States of $BiFeO_3$ Nanoparticles with Promising Photocatalytic Performance in Dye Degradation. *J. Phys. Chem. Solids* **2021**, *152* (January), 109926.
(25) Berglund, S. P.; Abdi, F. F.; Bogdanoff, P.; Chemseddine, A.; Friedrich, D.; Van De Krol, R. Comprehensive Evaluation of $CuBi_2O_4$ as a Photocathode Material for Photoelectrochemical Water Splitting. *Chem. Mater.* **2016**, *28* (12), 4231−4242.
(26) Liu, Z.; Qi, Æ. Y.; Lu, Æ. C. High Efficient Ultraviolet Photocatalytic Activity of $BiFeO_3$ Nanoparticles Synthesized by a Chemical Coprecipitation Process. **2010**, *21*, 380−384. .
(27) Srivastav, S. K.; Gajbhiye, N. S. Low Temperature Synthesis, Structural, Optical and Magnetic Properties of Bismuth Ferrite Nanoparticles. *J. Am. Ceram. Soc.* **2012**, *95* (11), 3678−3682.
(28) Zatsiupa, A. A.; Bashkirov, L. A.; Troyanchuk, I. O.; Petrov, G. S.; Galyas, A. I.; Lobanovsky, L.; Truhanov, S. Journal of Solid State Chemistry Magnetization, Magnetic Susceptibility, Effective Magnetic Moment of Fe^{3+} Ions in $Bi_{25}FeO_{39}$ Ferrite. *J. Solid State Chem.* **2014**, *212*, 147−150.
(29) Wu, T.; Liu, L.; Pi, M.; Zhang, D.; Chen, S. Enhanced Magnetic and Photocatalytic Properties of $Bi_2Fe_4O_9$ Semiconductor with Large Exposed (001) Surface. *Appl. Surf. Sci.* **2016**, *377*, 253−261.
(30) Lafta, S. H. The Relation of Crystallite Size and Ni2 + Content to Ferromagnetic Resonance Properties of Nano Nickel Ferrites The Relation of Crystallite Size and Ni^{2+} Content to Ferromagnetic Resonance Properties of Nano Nickel Ferrites. **2017**, No. *22*, 2. 188, 195, .
(31) Jia, Y.; Wu, C.; Kim, D. H.; Lee, B. W.; Rhee, S. J.; Park, Y. C.; Kim, C. S.; Wang, Q. J.; Liu, C. Nitrogen Doped $BiFeO_3$ with Enhanced Magnetic Properties and Photo-Fenton Catalytic Activity for Degradation of Bisphenol A under Visible Light. *Chem. Eng. J.* **2018**, *337*, 709−721.
(32) Di, L.; Yang, H.; Xian, T.; Liu, X.; Chen, X. Photocatalytic and Photo-Fenton Catalytic Degradation Activities of Z-Scheme Ag_2S/$BiFeO_3$ Heterojunction Composites under Visible-Light Irradiation. *Nanomaterials* **2019**, *9* (3), 399.
(33) Vavilapalli, D. S.; Melvin, A. A.; Kavita, S.; Yadav, A. K.; Jha, S. N.; Bhattacharyya, D.; Sarma, S. C.; Peter, S. C.; Ramachandra Rao, M. S.; Singh, S. Multifunctional Brownmillerite $KBiFe_2O_5$: Structural, Magneto-Dielectric, Optical, Photoelectrochemical Studies and Enhanced Photocatalytic Activity over Perovskite $BiFeO_3$. *Sol. Energy Mater. Sol. Cells* **2019**, *200* (January), 109940.
(34) Jangid, S.; Barbar, S. K.; Bala, I.; Roy, M. Structural, Thermal, Electrical and Magnetic Properties of Pure and 50% La Doped $BiFeO_3$ Ceramics. *Phys. B* **2012**, *407* (18), 3694−3699.
(35) Khajonrit, J.; Phumying, S.; Maensiri, S. Structure and Magnetic/Electrochemical Properties of Cu-Doped $BiFeO_3$ Nanoparticles Prepared by a Simple Solution Method Structure and Magnetic/Electrochemical Properties of Cu-Doped $BiFeO_3$. *Jpn. J. Appl. Phys.* **2016**, *55*, 06GJ14.
(36) Li, L.; Kler, J.; Sinclair, D. C.; West, A. R.; Deouza, R. A. High oxide-ion conductivity in acceptor-doped Bi-based perovskites at modest doping levels. **2021**, *23*, 11327−11333. .
(37) Madavali, B.; Kim, H.; Lee, K.; Hong, S. Intermetallics Enhanced Seebeck Coef Fi Cient by Energy Fi Ltering in Bi-Sb-Te Based Composites with Dispersed Y_2O_3 Nanoparticles. *Intermetallics* **2017**, *82*, 68−75.
(38) Mun, H.; Choi, S. M.; Lee, K. H.; Kim, S. W. Boundary Engineering for the Thermoelectric Performance of Bulk Alloys Based on Bismuth Telluride. *ChemSusChem* **2015**, *8* (14), 2312−2326.
(39) Pei, J.; Zhang, L. J.; Zhang, B. P.; Shang, P. P.; Liu, Y. C. Enhancing the Thermoelectric Performance of $Ce_xBi_2S_3$ by Optimizing the Carrier Concentration Combined with Band Engineering. *J. Mater. Chem. C* **2017**, *5* (47), 12492−12499.
(40) Liu, Z.; Pei, Y.; Geng, H.; Zhou, J.; Meng, X.; Cai, W.; Liu, W.; Sui, J. Enhanced Thermoelectric Performance of Bi_2S_3 by Synergistical Action of Bromine Substitution and Copper Nanoparticles. *Nano Energy* **2015**, *13*, 554−562.

https://doi.org/10.1021/acsomega.4c05361
ACS Omega 2024, 9, 35088−35099